7
Stress-Driven Nanopatterning in Metallic Systems

Vincent Repain, Sylvie Rousset, and Shobhana Narasimhan

7.1
Introduction

The desire to gain a fundamental understanding of the physical properties of nanostructures down to the atomic limit, as well as a host of practical applications, drives the need for achieving uniform arrays of nanostructures. Since standard lithography techniques are intrinsically limited in resolution, new physical methods have to be used. Epitaxial growth has been shown to be an interesting alternative, as thermodynamic or kinetic processes can be involved to get uniform nanostructures on surfaces [1]. From a kinetic point of view, the self-assembly of nanoislands by nucleation on surfaces [2, 3] has proved to be a solution to randomly grow nanostructures with an adjustable size and density. However, the size distributions are always broad. To overcome this drawback, the use of prestructured templates has been proposed that effectively provides an ordered growth regime under adequate flux and temperature conditions [4, 5]. One of the difficulties of such a technique is the ability to realize and control a regular surface pattern at nanometer scale. Fortunately, the presence of surface stress, and the processes that take place to minimize its contribution to the total energy, can lead to such natural surface patterning at nanometer length scales, either in homoepitaxial or in heteroepitaxial systems. Once again, the interest of such surfaces for applications comes from their ability to serve as templates for the growth of ordered nanostructures. By such a bottom-up technique, state-of-the-art arrays of monodisperse nanoparticles, as small as tens of atoms each, have been realized in the past two decades and subsequently used for the study of their physical properties. In this chapter, we review such phenomena, restricting ourselves primarily to metallic systems, including alloys. The study of such self-organized systems is basically divided into two different parts. In the first one, where surface stress plays a major role, the goal is to understand and predict the equilibrium morphology of surfaces at the nanometer scale. In the second one, this nanopatterning is exploited to grow nanostructures; their size, shape, and density are generally driven by a combination of local thermodynamic and kinetic

Mechanical Stress on the Nanoscale: Simulation, Material Systems and Characterization Techniques, First Edition. Edited by Margrit Hanbücken, Pierre Müller, and Ralf B. Wehrspohn.

processes. At present, a variety of experimental and theoretical techniques are available to study such phenomena. However, from an experimental point of view, the invention of scanning probe microscopies, and more particularly of scanning tunneling microscopy, has been a crucial step in the systematic study of metallic crystalline self-organized surfaces and nanostructures. During the 1990s, pioneering groups discovered periodic patterns such as the herringbone reconstruction of Au (111) [6] and the CuO stripes on Cu(110) [7] and showed their ability to serve as templates for subsequent ordered growth [8]. To describe such phenomena theoretically, there is a hierarchy of possible approaches. The most accurate approach would be to perform *ab initio* density functional theory calculations. Surface stress can be calculated reliably and efficiently, making use of the Nielsen–Martin stress theorem [9]. However, the disadvantage of this approach is that one is restricted to fairly small length scales because of issues of computational cost. At larger length scales, one can make use of semiempirical potentials such as those obtained using the embedded atom model [10], effective medium theory [11], or the glue model [12]; these are considerably cheaper than first-principles calculations but not always reliable. Finally, to extend to large length scales, one can go over to descriptions using continuum elasticity theory. One very useful classical model, which helps one understand qualitatively many of the stress-driven phenomena that occur at surfaces, is the Frenkel–Kontorova model [13] (and subsequent generalizations of it). A successful modern approach has been to use this time-tested model, however, with the parameters in it obtained from *ab initio* density functional theory calculations. In many cases, the results thus obtained have been in remarkably good agreement with experiments.

7.2
Surface Stress as a Driving Force for Patterning at Nanometer Length Scales

7.2.1
Surface Stress

The concepts of surface energy and surface stress date back to the pioneering work of Gibbs [14], developed further by Shuttleworth [15] and Herring [16]. The surface stress tensor $\sigma_{\alpha\beta}$ is defined by

$$\sigma_{\alpha\beta} = \gamma\delta_{\alpha\beta} + \frac{\partial\gamma}{\partial\varepsilon_{\alpha\beta}} \tag{7.1}$$

where $\varepsilon_{\alpha\beta}$ is the strain tensor, $\delta_{\alpha\beta}$ is the Kronecker delta, and γ is the surface free energy per unit area. For a more detailed discussion of the surface stress, we refer the reader to Chapter 2. Even for a situation where the surface energy is minimized, the surface stress is in general not zero and may be tensile or compressive, indicating that the surface atoms would like to increase or decrease their density [17]. In general, the stress at a bulk-truncated metallic surface is tensile; this is because surface atoms have lost their neighbors in the layers above and would therefore like to come closer to

their neighbors in the surface layer so as to be embedded in an optimal ambient electronic density. For heteroepitaxial metallic systems, the surface stress may be compressive or tensile, depending on the size mismatch between overlayer and substrate atoms. If the size of overlayer atoms is smaller or larger than that of the substrate, then one would expect the surface stress to be tensile or compressive, respectively. However, one should note that the "size" of an atom is not necessarily a simple concept; in particular, the effective size of an atom at the surface may differ considerably from that of a bulk atom. If the magnitude of the surface stress is large, it can serve as a driving force for reconstruction or alloying. In the former case, the density of atoms in the surface layer changes, thereby reducing the surface stress. In the latter case, atoms in the overlayer mix with those of the substrate, or two overlayer species mix on the substrate (even, in some cases, if they are bulk immiscible), thus reducing the magnitude of the surface stress. All these phenomena lead to patterning at nanometer length scales, as we will describe later.

7.2.2 Surface Reconstruction and Misfit Dislocations

7.2.2.1 Homoepitaxial Surfaces

For simplicity of discussion, let us first consider a homoepitaxial system and assume that the surface stress is tensile, as is generally the case for metallic systems. As discussed previously, as a result of this tensile stress, surface atoms would like to increase their density. However, this tendency is opposed by the presence of the substrate. These two opposing factors are accounted for by the two main terms in the Frenkel–Kontorova model. In its original form, this model consists of a linear chain of atoms (the surface layer) connected by harmonic springs, sitting in a sinusoidal potential that represents the effect of the substrate (Figure 7.1). There are two competing periodicities in the system: the preferred length of the springs (the favored nearest-neighbor spacing of the surface layer alone) is less than the distance between neighboring minima of the substrate potential (which corresponds to the lattice spacing of the substrate). The advantage of the original form of the Frenkel–Kontorova model is that it can be solved analytically; however, it is simple to generalize it to two dimensions and other forms of potentials, in which case the model can be solved

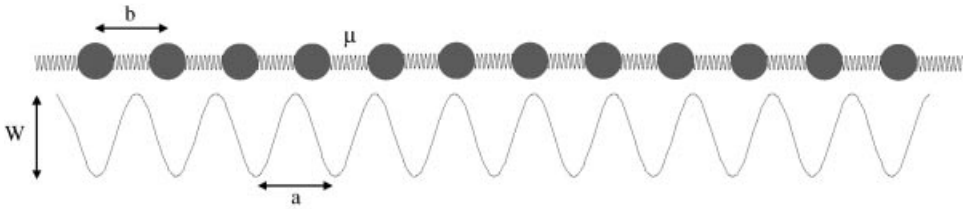

Figure 7.1 Schematic diagram of the Frenkel–Kontorova model. The sine potential of depth W and period a (bulk lattice spacing) represents the substrate atoms. The surface atoms are connected by springs of natural length b (surface lattice spacing) and spring constant μ.

numerically so as to obtain the ground state configuration. In cases where the springs are sufficiently stiff to overcome the effects of the substrate potential, the surface layer reconstructs typically in a pattern such that regions where the surface layer remains in registry with the substrate are separated by misfit dislocations where the density is locally increased. Other possibilities are Moiré patterns where the surface grid has a more or less uniformly increased density relative to that of the substrate; it may also happen that the symmetry of the overlayer grid may be different from that of the substrate—for example, the substrate may have square symmetry while the overlayer may have hexagonal symmetry. The best-known example of a system that displays such a reconstruction, driven by stress relief, is the Au(111) surface. There have been several calculations of the stress on the unreconstructed Au(111) surface [18]. Although there is some variation in the numbers obtained, all the calculations agree that there is a considerable tensile stress on this surface. As an example, in a recent calculation, we obtained a value of 3.6 N/m (we note that *ab initio* calculations of surface stress are notoriously difficult to converge, both with respect to basis size and with respect to the number of layers used in simulating a surface slab, explaining a relative dispersion of values obtained in different calculations) [19]. There are two low-energy stacking sites for Au atoms in the topmost layer: face-centered cubic (fcc) and hexagonal close packed (hcp). Domains of the two types of stacking are separated by misfit dislocations where surface atoms occupy the bridge sites that lie between the fcc and hcp sites [20–22]; these show up clearly as light stripes in scanning tunneling microscopy images. As a result of alternating between occupying the two types of stacking sites, the surface layer densifies by 4%, thereby reducing the tensile stress. The resulting pattern has a repeat distance of 22 nearest-neighbor spacings, which is about 63 Å. It is worth noting that the Au(100) surface also displays a surface reconstruction with a large unit cell. In this case, the substrate has square symmetry, whereas the overlayer has triangular symmetry, resulting in a (26×48) unit cell [20]. Another homoepitaxial system that displays a reconstruction driven by stress relief is Pt(111). While this is similar to Au(111) in that Pt and Au are both fcc metals, the reconstruction differs in two ways: (i) the Au(111) surface nearly always displays a reconstruction, but Pt(111) displays a reconstruction only at high temperatures [23] or in the presence of a supersaturated Pt vapor [24]; (ii) in the case of Au(111), the densification takes place along only one direction in the surface plane, whereas in the case of Pt(111), there is an increase in density along three equivalent directions in the surface plane. In Figure 7.2, we have shown simulated STM images that show how the repeat distance and the pattern change on increasing the densification in the top layer relative to the substrate; it is possible to control this parameter by tuning the temperature or the chemical potential [25]. Mansfield and Needs mapped real surfaces onto the exactly solvable one-dimensional Frenkel–Kontorova model in a simple way and showed that a dimensionless parameter that involved combinations of the surface stress, surface energy, surface lattice constant, stacking fault energy, and stiffness of nearest-neighbor bonds (these parameters can all be estimated from *ab initio* density functional theory calculations) could be used to predict whether a metallic surface will reconstruct [26]. Subsequent authors have shown that this simple model works surprisingly well for the (111) surfaces of fcc metals [25, 27].

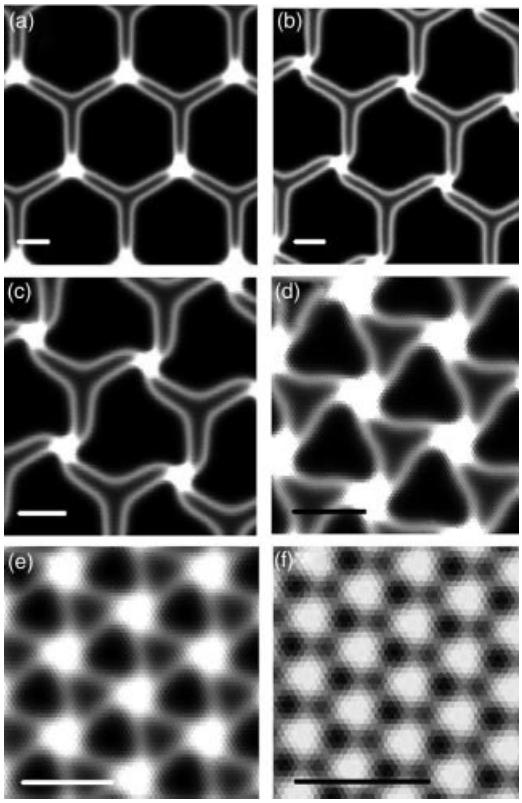

Figure 7.2 Simulated STM images of a reconstructed Pt(111) surface. Between (a), (b), and (e), the enhanced density in the surface layer, relative to the substrate, is progressively increased from 2.9% to 21%. In (a), a rotation of the surface layer relative to the substrate is not permitted, and in all other cases, it is permitted. The white/black line in each image represents a length of 50 Å, and note that the patterns have nanometer spacing.

7.2.2.2 **Heteroepitaxial Systems**

Heteroepitaxial systems display reconstruction phenomena similar to those observed on homoepitaxial systems, with the difference that the stress can be tensile or compressive, and therefore the reconstruction can be compressive or expansive, respectively. The stress builds up with the number of overlayers deposited. Typically, with the deposition of the first monolayer, the stress is not sufficient to trigger a reconstruction, and the system remains pseudomorphic (i.e., the overlayer remains in registry with the substrate). Progressively more "drastic" reconstructions are observed as further layers are deposited, for example, if one considers Cu/Ru(0001): here, the lattice spacing of the overlayer, Cu, is 5.5% smaller than that of the substrate, Ru. The first monolayer goes down pseudomorphically, the bilayer shows a striped reconstruction similar to that observed on Au(111), the trilayer shows a triangular pattern (similar to Figure 7.2d or e),

while for four or more Cu layers, a Moiré pattern (similar to Figure 7.2f) is observed) [28]. A similar sequence of patterns has also been observed in theoretical modeling of this system [29]. The Ag/Ru(0001) system differs in that the lattice constant of Ag is larger than that of Ru, and the unreconstructed surface therefore exhibits a compressive stress. This system also relaxes through the formation of misfit dislocations, similar to those observed on Au(111), with the difference that in this case these misfit dislocations correspond to regions of rarefaction rather than densification [30]. Another compressively stressed system that shows stress-driven reconstruction is Ag/Pt(111). Once again, the first monolayer remains pseudomorphic, while the second monolayer displays a reconstruction. At first, there is a metastable striped reconstruction, similar to that observed on Au(111) (except, of course, that it corresponds to rarefaction rather than densification); upon annealing, it is transformed into a trigonal network of domain walls [31].

7.2.3
Stress Domains

It is important to keep in mind that the surface stress is a tensor and not a scalar. When the surface reconstructs by densifying or rarefying along only one direction in the surface plane (as is the case for the various striped reconstructions described above, such as that of Au(111)), stress is relieved (partially) along only that direction, resulting in an anisotropic surface stress tensor. Note that in the case of Au(111), the surface plane has threefold symmetry, and therefore this densification could have occurred along any one of three equivalent directions. When there is an anisotropic surface stress tensor, and a degeneracy of directions along which it can be oriented, it has been shown by the theory of "stress domains" of Marchenko [32] and Alerhand *et al.* [33] that the lowest energy situation will always correspond to a regular alternation between domains of different orientations; it is possible to estimate the domain width from continuum elasticity theory. Indeed, this is what appears to happen in the case of Au(111): the striped pattern alternates periodically between two out of the possible three orientations, resulting in the famous "herringbone" or "chevron" reconstruction (Figure 7.3a) [6, 34, 35]. At alternating "elbows," where there are bends in the soliton walls that follow the lines of the misfit dislocations, there are point dislocations, where the atoms have five to seven coordination instead of the sixfold coordination characteristic of the fcc(111) surface. These serve as nucleation sites for the growth of overlayers and constitute a regularly spaced two-dimensional grid, since the herringbone pattern is periodic. Thus, the herringbone pattern constitutes a convenient template for the growth of self-organized nanostructures and has frequently been used as such. The same "stress domains" physics can appear in the case of adsorbates on surfaces. Among many examples, Figure 7.3b shows the self-organization of a partially oxygen covered Cu(110) surface [7]. Such a system is simply realized by a controlled adsorption of O_2 onto the surface and a subsequent annealing. The natural anisotropy of the (110) surface leads here to a one-dimensional pattern with a nanometer-scale period. On a more isotropic surface,

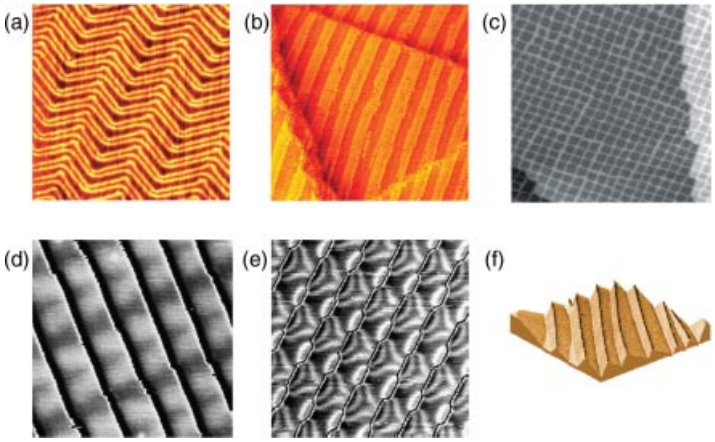

Figure 7.3 STM images of self-organized surfaces with periodic nanometer-scale patterns. (a) Herringbone reconstruction of the Au(111) surface. The typical periodicity is 30 nm. (b) CuO stripes on a Cu(110) surface. Courtesy of Peter Zeppenfeld. The periodicity is around 6 nm. (c) CuN islands on a Cu(100) surface. The periodicity is around 5 nm. (d) Reconstruction of the Au(788) vicinal surface that defines a two-dimensional pattern with step edges of dimensions $7.2 \times 3.8\ nm^2$. (e) Reconstruction of a Au vicinal surfaces with 8 nm wide terraces. The interplay between step edges and the strain-relief pattern induces a complex morphology. (f) Faceted Au(455) vicinal surface. The typical periodicity is around 200 nm.

such as the Cu(100) surface, two-dimensional self-organization can be observed, as shown in Figure 7.3c with the checkerboard arrangement of 5 nm CuN islands [36].

7.2.4 Vicinal Surfaces

It has been shown previously that some flat surfaces of homoepitaxial or heteroepitaxial metallic systems can display strained-relief patterned substrates such as dislocation networks that can be subsequently used for the growth of uniform nanoparticles. However, intrinsic defects such as step edges prevent the achievement of long-range ordered arrays of nanostructures since the presence of atomic steps generally limits the coherence of the surface dislocation networks. Steps can also act as nucleation sites for the growth of uncontrolled elongated clusters. Since macroscopic averaging methods are still commonly used for measuring physical properties of nanostructures, these defects are major drawbacks of such bottom-up techniques. To overcome these difficulties, a novel approach has been investigated using strained-relief vicinal patterned substrates to achieve a high degree of both local and long-range order for the growth of nanostructures. Vicinal surfaces, also called stepped surfaces, display a one-dimensional network of atomic steps separating terraces. The choice of the miscut angle of such a surface compared to a flat surface allows one to control the mean width of terraces. The narrowness of the terrace width distribution is mainly driven by the elastic step–step interaction strongly related to the value of

surface stress, as demonstrated both theoretically and experimentally on various systems [19] (for a detailed description of this interaction, refer to Chapter 13). Generally, vicinal surfaces offer a one-dimensional pattern that can serve as a template for the growth of one-dimensional nanostructures down to atomic wires [37]. However, the combination of the atomic step network and strain-relief patterns such as dislocation networks can lead to highly uniform two-dimensional template surfaces. Well-studied examples of such systems are the Au(111) vicinal surfaces. As discussed previously, the Au(111) surface is one of the famous examples of natural strain-relief patterns with its herringbone reconstruction. Its vicinal surfaces also show a variety of surface reconstructions with the particular features of very good long-range order and an extremely low density of defects. Figure 7.3d and e show STM images of two of these surfaces that have been shown to be useful for the growth of regular nanostructures. Among them, the Au(788) surface has been the most studied, with the demonstration of the growth of regular nanoparticles of Co, Fe, Ag, and C_{60} [41, 49–51]. The shapes of strain-relief patterns on vicinal surfaces are generally complex to simulate, due to an interplay between step edge and surface energies. In the case of Au(111) vicinal surfaces, basic arguments have been put forward to explain the shape of certain surface reconstructions and their influence on the stability of such surfaces [38, 39]. An example of an unstable vicinal surface is shown in Figure 7.3f. This faceted Au(455) surface constitutes once again an example of a self-organized system with a 200 nm period driven by the difference of surface stress between the two facets.

7.3
Nanopatterned Surfaces as Templates for the Ordered Growth of Functionalized Nanostructures

7.3.1
Metallic Ordered Growth on Nanopatterned Surface

7.3.1.1 Introduction

Nowadays, naturally patterned surfaces are successfully used as templates to grow ordered nanostructures from metallic nanodots [40] to molecular assemblies [41] with controlled size and density. As shown previously, a broad range of materials can display mesoscopic periodic surface patterns and can therefore be suitable for ordered growth. Most of the early studies have focused on metallic surfaces [40] with the well-known Au(111) reconstructed surface [8], but spectacular results have also been demonstrated on semiconductors [42, 43], on insulating layers [44], and more recently on supported graphene layers [45, 46]. This last system can display a single domain Moiré pattern over at least several micrometers scale, irrespective of surface defects such as step edges [47]. This improves the long-range order and the uniformity of nanostructures, which is necessary to study their physical properties measured by averaging techniques [48] and to predict possible technological applications. As explained previously, the use of reconstructed vicinal surfaces has also been

shown to increase the long-range order of these arrays of nanostructures over macroscopic scale [49]. For example, the Au(788) surface has been used for the growth of two-dimensional lattices of Co [49], C_{60} [41], Ag and Cu [50], Fe [51], and so on. The atomistic mechanisms responsible for ordered growth have been studied in detail in specific cases [40, 52] and the temperature dependence of the growth on patterned substrates has been analyzed [53]. In the following, we explain the basic concepts leading to ordered growth and our actual understanding of such phenomena. It is worth noting that an important condition to obtain ordered growth is that the surface patterns should remain unaffected by the growth process. Considering the complexity of surface science phenomena, this latter point is not trivial and generally difficult to predict. This hypothesis will be assumed to be true in the following. However, a few examples of self-organized surfaces modified during the growth of nanostructures have been reported [54, 55].

7.3.1.2 Nucleation and Growth Concepts

Nucleation and growth of islands on surfaces has been extensively studied for many years and has been reviewed in several articles and books [40, 56]. Atoms are deposited from a vapor pressure onto a surface, such as in the common case of solid on solid model. In the case of adatoms moving on a homogeneous substrate (which is called homogeneous growth), the process is well described by mean field theory and is essentially determined by atomistic parameters for surface diffusion and binding energies of adatoms to clusters. Values for these parameters may be determined by comparing scaling predictions with suitable experimental measurements [57]. One usually distinguishes three regimes versus the coverage of deposited atoms: the nucleation regime where the density of stable islands is increased, the growth regime where the density is almost constant but the size of islands increases, and the coalescence regime where the density of islands decreases since neighboring islands start to coalesce. The maximum cluster density versus the temperature can be determined from variable temperature STM experiments. In the regime of complete condensation generally relevant for metal on metal growth, re-evaporation of adatoms from the substrate into the vapor is negligible. The maximum cluster density n_c is given by

$$n_c = \eta(D_0/F)^{-1/3}\exp(E_{diff}/3k_BT) \tag{7.2}$$

where η is a prefactor related to capture numbers, F is the deposition rate (flux), D_0 is the diffusion prefactor, and E_{diff} is the diffusion energy. This expression is valid in the case of stable dimers on the surface, that is, critical cluster size $i = 1$ (i is defined as the size of the biggest unstable cluster). In the case of $i > 1$, Eq. (7.2) should be modified and involves the binding energy of the critical cluster. In the simple $i = 1$ regime, it is worth noticing that the slope of n_c versus T in an Arrhenius plot gives E_{diff}. At higher temperature, the critical nucleus size increases and this leads to a higher slope. Such behavior is also found by using kinetic Monte Carlo (KMC) simulations. The advantage of a KMC simulation is that it goes beyond the mean field approximation that is known, for example, to overestimate the island density.

7.3.1.3 Heterogeneous Growth

What happens now when all atomic sites onto the substrate are not equivalent, such as on the self-organized surfaces described in Section 7.2? Some sites can act as preferential nucleation sites, such as, for example, the point dislocations located at the elbows of the Au(111) herringbone reconstruction. These sites can be described in a mean field model as traps for adatoms [58, 59]. Such a model had some success in the past by reproducing the nucleation and growth on surfaces with point defects [60, 61]. We show here how it can be applied nicely to growth on self-organized surfaces [52]. A typical theoretical curve of the critical cluster density versus the temperature is shown in Figure 7.4b [53, 56]. For the lowest temperature, no variation is found: the cluster density is constant with temperature. This corresponds to a low diffusion regime called "postnucleation" [40] when adatoms hardly diffuse on the surface and are stable. Between 45 and 80 K, a linear decrease in the cluster density with temperature in an Arrhenius plot is found. At such low temperatures, the mean free path of adatoms on the surface is lower than the mean

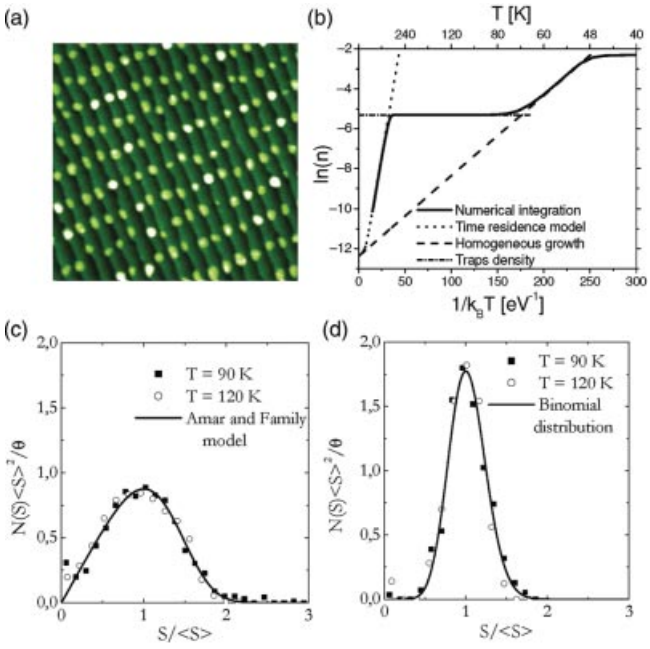

Figure 7.4 (a) STM image of an ordered growth of Co nanodots on a Au(788) surface. (b) Arrhenius plot of the island density (in islands/atomic sites) versus temperature calculated by numerical integration of rate equations in a point defect model. The analytical asymptotic regimes are also plotted (cf. text). (c) Size distributions calculated by KMC for growth on a homogeneous substrate at 90 and 120 K ($\theta = 0.1$ ML). The solid line shows the Amar and Family model. (d) Size distributions calculated by KMC for the growth on a heterogeneous substrate with a periodic array of atomic traps at 90 and 120 K ($\theta = 0.1$ ML). The solid line shows the binomial distribution associated with the Voronoï area of the trap lattice.

distance between traps. This regime is identical to the homogeneous growth, and the slope of the Arrhenius plot is E_{diff}. Above the temperature threshold T_0, the system displays the ordered growth regime. The maximum cluster density is constant, equal to the density of traps. T_0 is the temperature at which the adatoms' mean free path determined by Eq. (7.2) is equal to the distance between traps. As a consequence, the parameters that determine T_0 are E_{diff} and the trap density n_{t}. Ordered growth occurs as long as the typical energies of the trapping mechanisms are sufficient to stabilize adatoms in the traps. We call T_{e} the highest temperature for which an ordered growth is observed. The crucial parameter, which determines T_{e}, is the trap energy E_{t}. Above T_{e}, the critical island density decreases dramatically with temperature. The slope is higher than a simple homogeneous growth regime. Such a high value is mainly due to the long time spent by adatoms in traps. The effect of traps is then to reduce the effective diffusion of adatoms [53]. Eventually, the mean field calculations including traps give a qualitative understanding of the ordered growth. Rapid adatom diffusion and strong trapping are the main ingredients needed to get an ordered growth over a large temperature range. We now focus on the other key point of ordered growth, which is the achievement of narrow size distributions. Unfortunately, the mean field approach of the previous mean field model cannot give any idea about the island size fluctuations during the nucleation and growth processes. Although a phenomenological model has been proposed for homogeneous growth by Amar and Family [62], very little is known for the growth on heterogeneous substrates, especially for ordered growth. To obtain some information on these size distributions, KMC simulations can be performed [53]. Some results of these simulations are shown in Figure 7.4c and d, which correspond to the case of an homogeneous surface and a surface prestructured with a rectangular array of traps, respectively. The homogeneous growth size distributions are perfectly reproduced by the Amar and Family model [62] and show typical full widths at half maximum (FWHM) of 110% whatever the temperature. In the case of the growth on the prestructured surface, when nucleation occurs on the traps ($T_0 < T < T_{\mathrm{e}}$), the size distributions are narrower and almost constant with temperature in this range. The FWHM for $n_{\mathrm{t}} = 1/200$ and $\theta = 0.1$ MC is typically 50%. Interestingly, these size distributions are very well fitted by simple binomial distributions $p(k) = C_k^n \theta^k (1-\theta)^{n-k}$, with k the island size (in number of atoms) and n the number of atomic sites of the Voronoï area in the trap lattice (i.e., $n = 1/n_{\mathrm{t}}$). This fact has already been pointed out for the ordered growth of Ag/Ag(2 ML)/Pt(111) [4] but is less trivial for growth induced by point defect nucleation. This means that during the growth regime, the probability that an adatom deposited on the surface does not stick to its closest island is vanishingly small, whatever the coverage or the temperature between T_0 and T_{e}, at least for the parameters used in our simulations. Moreover, simulations on randomly distributed atomic traps show a broadening of the island size distribution due to the distribution of traps Voronoï area. This confirms that the analysis of size distributions in terms of the Voronoï area distribution is always pertinent. Therefore, the FWHM of the size distribution is limited to the perfectness of the traps array for a given coverage. In addition, even for a perfect trap array, there is an intrinsic statistical limit to the size distribution width. As for the binomial distribution,

the variance is $\sigma = \sqrt{(1-\theta)/n\theta}$, the only way to improve the size distribution quality is to increase the coverage and use a surface with a lower trap density (larger Voronoï cells).

7.4 Stress Relaxation by the Formation of Surface-Confined Alloys

Stress effects play also an important role in the process of alloying. Already since ancient times, it has been known that alloying two metals can result in the formation of a new material with superior properties to that of the constituent metals. However, not all combinations of metals will form stable alloys; the empirical rules governing alloy formation were formulated by Hume-Rothery *et al.* [63]. The first of these rules states that if the size mismatch between the two metals is greater than 15%, then alloy formation is disfavored; this is because otherwise too much elastic strain builds up in the material. The surprising discovery in recent years has been that bulk-immiscible metals may, however, form surface-confined alloys. The driving force behind such surface alloying is generally believed to be stress relief, though, as we will discuss later, in some cases, such as when one of the constituents is a magnetic element, we have reason to believe that other mechanisms also play an important role.

7.4.1 Two-Component Systems

As an example, Au and Ni are immiscible in the bulk. However, when Au is deposited on Ni(110), surface alloying is observed [64]. This has been confirmed by calculations, making use of potentials derived from effective medium theory. There are many other such examples, such as Na/K on Al(111) and Al(100) [65], Ag on Pt(111) [66], and Sb on Ag(111) [67]. It has subsequently been shown by Tersoff [68] that one may expect to see such a phenomenon, in general, in systems dominated by size mismatch and in which, therefore, elastic stress plays a major role. The remarkable thing is that the same feature, atomic size mismatch, that prevents intermixing in the bulk actually promotes mixing at the surface. In some cases, such surface alloys are disordered; however, in other cases, they form ordered structures; long-range order is of interest for certain applications. Surface alloys, in general, offer possibilities as novel catalytic materials and (when one or more of the constituent metals is magnetic) materials for applications in nanomagnetism.

7.4.2 Three-Component Systems

One can also consider another type of surface alloy: one can codeposit two bulk-immiscible metals, A and B, on a substrate C of intermediate spacing. If A has a lattice constant smaller than that of C, while B has one larger than that of C, then an unreconstructed monolayer of A on C would display tensile stress, while a monolayer

of B on C would exhibit compressive stress. One might thus expect that stress relief might provide a driving force for mixing in such a system and one may obtain a surface alloy of A and B on C. Motivated by such considerations, Thayer *et al.* considered Co and Ag codeposited on a Ru(0001) substrate [69, 70]. Since the nearest-neighbor distance of Ag is larger than that of Ru by 8%, while that of Co is smaller than that of Ru by 7%, one might expect to find such surface alloy formation in this system. However, one does not find atomic-level mixing. Instead, for submonolayer films, one finds Ag droplets surrounded by a Co matrix. For larger Ag concentrations, the system forms a phase consisting of dislocated Ag/Ru(0001) and alloy droplets. The reason that there is no atomic level mixing is because elastic interactions alone do not determine the surface structure, one also has to take into account chemical interactions. The droplet size is determined by a balance between energy reduction due to stress reduction and the energetic cost of forming unfavorable chemical bonds.

A combinatorial study of small magnetic metals M alloyed with large nonmagnetic metals N on the Ru(0001) surface has recently been carried out using density functional theory techniques [71]. Among the results that emerged from this study, we mention that (i) several bulk-immiscible M-N pairs were found to atomically mix on the surface, (ii) atomic sizes at the surface were sometimes significantly different from bulk sizes, (iii) both elastic and chemical interactions were found to be important, and (iv) no simple size-dependent criterion emerged in predicting mixing; this is because unlike the bulk case, in the surface case the phase segregated forms contain large elastic energy. As a result of this study, Fe-Au/Ru(0001) was identified as a promising candidate to observe a long-range ordered surface alloy, even though Fe and Au are bulk immiscible. Indeed, using STM and low-energy electron diffraction (LEED) experiment, we have discovered a new ordered surface alloy made out of Fe and Au, deposited on a Ru(0001) substrate. The alloy films were prepared by depositing one metal, annealing, and repeating the same procedure for the second metal; in this way, large islands were obtained. Au was deposited from an e-beam heated Mo crucible at the rate of 0.04 ML/min and Fe was deposited from an e-beam heated Fe rod at the rate of 0.07 ML/min. Evaporation rates were determined by analyzing the STM images giving rise to a typical error bar for the concentration x of around 5%. It is worth noting that the final results were found to be independent of whether Fe or Au was deposited first, demonstrating that we indeed reached the equilibrium configuration. For alternate deposition where the Fe fraction x is close to 0.33, we obtain a periodic structure as shown in Figure 7.5d. Although we can observe some local defects due to an imperfect 1 : 2 stoichiometry, there is relatively good long-range order, giving rise to a clear LEED diffraction pattern, characteristic of a $\sqrt{3} \times \sqrt{3}$ unit cell. This structure is the simplest two-dimensional ordered phase on a hexagonal lattice for the 1 : 2 stoichiometry. Simulation of constant height STM image calculated from *ab initio* data strongly supports the observed structure of the alloy, showing that Fe is imaged lower than Au, in good agreement with the experiments.

To get a deeper understanding of the driving forces that stabilized these pseudomorphic alloyed phases, we have performed spin polarized *ab initio* density functional theory calculations for several different configurations and compositions of

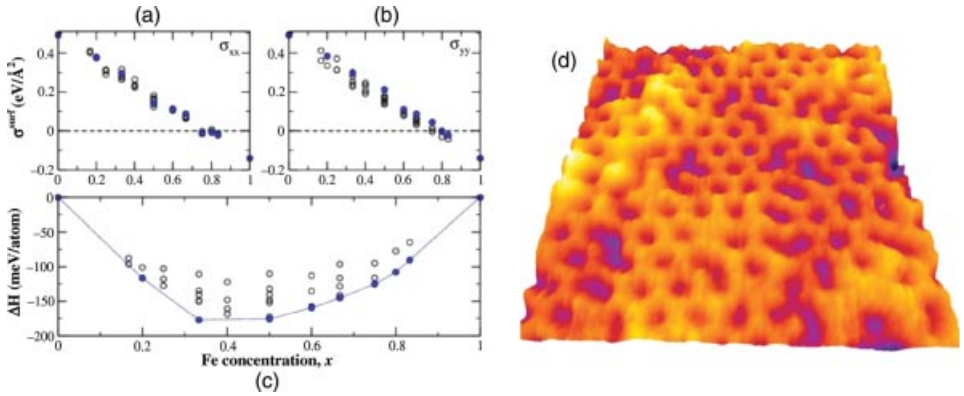

Figure 7.5 *Ab initio* results for (a) the *xx* component of the surface stress, (b) the *yy* component of the surface stress, and (c) the enthalpy of mixing ΔH, for Fe_xAu_{1-x}/Ru(0001), as a function of Fe concentration *x*. Forty-three different structures, containing up to six surface atoms per unit cell, have been considered. The blue line represents the convex hull and the blue dots represent stable alloy phases that lie on the convex hull. (d) $2.1 \times 2.1\,nm^2$ STM image of 0.9 ML coverage of $Fe_{0.33}Au_{0.67}$ deposition, after annealing at 600 K. Fe atoms are seen in darker dots located at the center of hexagons made up of lighter dots that are Au atoms.

this system. These calculations have confirmed that mixing is favored in this system and that the stress is indeed reduced on mixing (Figure 7.5a and b). Note that the stress for a pure monolayer of Au on Ru(0001) is compressive, while for a pure monolayer of Fe/Ru(0001) is tensile and for intermediate compositions, the surface stress is reduced, following an almost linear trend. However, these results hint at the fact that surface stress may not, surprisingly, be the dominant mechanism in this system, since the enthalpy of mixing ΔH shown in Figure 7.5c (which determines alloy stability) is lowest for an Au-rich phase, and not for Fe-rich phases, whereas the surface stress appears to go to zero under Fe-rich conditions at $x \simeq 0.8$. Moreover, the positions of the blue dots in Figure 7.5a and b indicate that the lowest energy configuration at a given value of Fe concentration *x* does not necessarily correspond to that with the lowest surface stress *x*. In fact, by performing additional calculations with the spin polarization suppressed, we have found that the principal driving force for mixing in this system is magnetism rather than stress relief. This surprising result explains the stability of the $\sqrt{3} \times \sqrt{3}$ structure of the long-range ordered surface alloy of $Fe_{0.33}Au_{0.67}$, which has been observed by STM and electron diffraction [72].

7.5 Conclusion

The realization and study of metallic nanostructures on surfaces is of particular importance for improved and innovative performances in various fields such as optics, magnetism, catalysis, and so on. We have shown in this chapter that a great

variety of metallic surfaces exhibit a nanoscale order at thermal equilibrium, including adsorbate-induced reconstruction, surface dislocation networks, vicinal surfaces, and more complex systems. Continuum models have been proposed where long-range elastic interactions induced by surface stress are responsible for spontaneous periodic domain formation. We have also discussed how these surfaces can be used as templates for ordered growth, which allows one to tailor a system with a very high density of monodisperse and regularly arranged nanostructures. The ordered growth usually appears within a temperature range for the temperature deposition, which is due to kinetically limited processes. A rate equation model modified to account for the preferred nucleation sites is generally able to qualitatively reproduce the epitaxial ordered growth behavior. However, microscopic mechanisms are complex and determined only by an extensive comparison between experiments and calculation. Eventually, by using both vicinal surfaces and strain-relief patterns, one can improve the two-dimensional long-range ordered growth of nanostructures. Concerning metallic alloys, we have recently discovered, by using epitaxial strain, a new ordered surface alloy made out of Fe and Au, two species largely immiscible in their bulk form. In this system, spin polarized *ab initio* calculations show that the most stable structures are always the ones with the highest magnetic moment per Fe atoms and not the ones minimizing the surface stress, in remarkable agreement with the observations.

Eventually, such a high quality of both long-range and local ordered growth opens up the possibility of making measurements of physical properties of such nanostructures by macroscopic integration techniques. This opens up novel possibilities for creating materials with unique properties of relevance to device applications.

Acknowledgment

Coworkers Cyril Chacon, Yann Girard, Mighfar Imam, Jérome Lagoute, Madhura Marathe, Shruti Mehendale, Stanislas Rohart, and David Vanderbilt who have contributed to this chapter are acknowledged. We acknowledge also funding from the Indo-French Center for the Promotion of Advanced Research, the Region Ile-de-France (SESAME), and the French Ministry of Research.

References

1 Shchukin, V.A., Ledentsov, N.N., and Bimberg, D. (2003) *Epitaxy of Nanostructures*, Springer, Berlin.
2 Röder, H., Hahn, E., Brune, H., Bucher, J.-P., and Kern, K. (1993) *Nature*, **366**, 141.
3 Teichert, C. (2002) *Phys. Rep.*, **365**, 335.
4 Brune, H., Giovannini, M., Bromann, K., and Kern, K. (1998) *Nature*, **394**, 451.
5 Leroy, F., Eymery, J., Gentile, P., and Fournel, F. (2002) *Appl. Phys. Lett.*, **80**, 3078.
6 Barth, J.V., Brune, H., Ertl, G., and Behm, R.J. (1990) *Phys. Rev. B*, **42**, 9307.
7 Kern, K., Niehus, H., Schatz, A., Zeppenfeld, P., Goerge, J., and Comsa, G. (1991) *Phys. Rev. Lett.*, **67**, 855.

8 Chambliss, D.D., Wilson, R.J., and Chiang, S. (1991) *Phys. Rev. Lett.*, **66**, 1721.
9 Nielsen, O.H. and Martin, R.M. (1983) *Phys. Rev. Lett.*, **50**, 697.
10 Daw, M.S. and Baskes, M. (1984) *Phys. Rev. B*, **29**, 6443.
11 Norskov, J.K. and Lang, N.D. (1980) *Phys. Rev. B*, **21**, 2131.
12 Ercolessi, F., Tosatti, E., and Parrinello, M. (1986) *Nature*, **322**, 769.
13 Frenkel, J. and Kontorova, T. (1938) *Phys. Z. Sowjetunion*, **13**, 1.
14 Gibbs, J.W. (1906) *The Scientific Papers of J. Willard Gibbs*, vol. 1, Longmans-Green, London.
15 Shuttleworth, R. (1950) *Proc. Phys. Soc. A*, **63**, 444.
16 Herring, C. (1953) *The Physics of Powder Metallurgy* (ed. W.E. Kingston), McGraw-Hill, New York.
17 Payne, M.C., Roberts, N., Needs, R.J., Needels, M., and Joannopoulous, J.D. (1989) *Surf. Sci.*, **211/212**, 1.
18 Needs, R.J. and Mansfield, M. (1989) *J. Phys. Condens. Matter*, **1**, 7555.
19 Prevot, G., Girard, Y., Repain, V., Rousset, S., Coati, A., Garreau, Y., Paul, J., Mammen, N., and Narasimhan, S. (2010) *Phys. Rev. B*, **81**, 075415.
20 Van Hove, M.A., Koestner, R.J., Stair, P.C., Biberian, J.P., Kesmodel, L.L., Bartos, I., and Somorjai, G.A. (1981) *Surf. Sci.*, **103**, 189.
21 Takayanagi, K. and Yagi, K. (1983) *Trans. Jpn. Inst. Met.*, **24**, 337.
22 Harten, U., Lahee, A.M., Toennies, J.P., and Woll, Ch. (1985) *Phys. Rev. Lett.*, **54**, 2619.
23 Sandy, A.R., Mochrie, S.G.J., Zehner, D.M., Gruebel, G., Huang, K.G., and Gibbs, D. (1993) *Phys. Rev. Lett.*, **G8**, 2192.
24 Bott, M., Hohage, M., Michely, T., and Comsa, G. (1993) *Phys. Rev. Lett.*, **70**, 1489.
25 Pushpa, R. and Narasimhan, S. (2003) *Phys. Rev. B*, **67**, 205418.
26 Mansfield, M. and Needs, R. (1990) *J. Phys. Condens. Matter*, **2**, 2361.
27 Crljen, Z., Lazic, P., Sokcevic, D., and Brako, R. (2003) *Phys. Rev. B*, **68**, 195411.
28 Gunther, C., Vrijmoeth, J., Hwang, R.Q., and Behm, R.J. (1995) *Phys. Rev. Lett.*, **74**, 754.
29 Hamilton, J.C. and Foiles, S.M. (1995) *Phys. Rev. Lett.*, **75**, 882.
30 Hwang, R.Q., Hamilton, J.C., Stevens, J.L., and Foiles, S.M. (1995) *Phys. Rev. Lett.*, **75**, 4242.
31 Brune, H., Roeder, H., Boragno, C., and Kern, K. (1994) *Phys. Rev. B*, **49**, 2997.
32 Marchenko, V.I. (1981) *Pis'ma Zh. Eksp. Teor. Fiz.*, **33**, 397 [*JETP Lett.*, 1981, 33, 381].
33 Alerhand, O.L., Vanderbilt, D., Meade, R.D., and Joannopoulos, J.D. (1988) *Phys. Rev. Lett.*, **61**, 1973.
34 Huang, K.G., Gibbs, D., Zehner, D.M., Sandy, A.R., and Mochrie, S.G.J. (1990) *Phys. Rev. Lett.*, **65**, 3313.
35 Narasimhan, S. and Vanderbilt, D. (1992) *Phys. Rev. Lett.*, **69**, 1564.
36 Ellmer, H., Repain, V., Rousset, S., Croset, B., Sotto, M., and Zeppenfeld, P. (2001) *Surf. Sci.*, **476**, 95.
37 Gambardella, P., Blanc, M., Brune, H., Kuhnke, K., and Kern, K. (2000) *Phys. Rev. B*, **61**, 2254.
38 Repain, V., Berroir, J.M., Croset, B., Rousset, S., Garreau, Y., Etgens, V.H., and Lecoeur, J. (2000) *Phys. Rev. Lett.*, **84**, 5367.
39 Rousset, S., Repain, V., Baudot, G., Garreau, Y., and Lecoeur, J. (2003) *J. Phys. Condens. Matter*, **15**, S3363.
40 Brune, H. (1998) *Surf. Sci. Rep.*, **31**, 121.
41 Néel, N., Kröger, J., and Berndt, R. (2006) *Adv. Mater.*, **18**, 174.
42 Li, J.-L., Jia, J.-F., Liang, X.-J., Liu, X., Wang, J.-Z., Xue, Q.-K., Li, Z.-Q., Tse, J.S., Zhang, Z., and Zhang, S.B. (2002) *Phys. Rev. Lett.*, **88**, 66101.
43 Sahaf, H., Léandri, C., Moyen, E., Macé, M., Masson, L., and Hanbücken, M. (2009) *Europhys. Lett.*, **86**, 28006.
44 Schmid, M., Kresse, G., Buchsbaum, A., Napetschnig, E., Gritschneder, S., Reichling, M., and Varga, P. (2007) *Phys. Rev. Lett.*, **99**, 196104.
45 N'Diaye, A.T., Bleikamp, S., Feibelman, P.J., and Michely, T. (2006) *Phys. Rev. Lett.*, **97**, 215501.
46 N'Diaye, A.T., Gerber, T., Busse, C., Mysliveček, J., Coraux, J., and Michely, T. (2009) *New J. Phys.*, **11**, 103045.
47 Coraux, J., N'Diaye, A.T., Busse, C., and Michely, T. (2008) *Nano Lett.*, **8**, 565.

48 Weiss, N., Cren, T., Epple, M., Rusponi, S., Baudot, G., Rohart, S., Tejeda, A., Repain, V., Rousset, S., Ohresser, P., Scheurer, F., Bencok, P., and Brune, H. (2005) *Phys. Rev. Lett.*, **95**, 157204.

49 Repain, V., Baudot, G., Ellmer, H., and Rousset, S. (2002) *Europhys. Lett.*, **58**, 730.

50 Didiot, C., Pons, S., Kierren, B., Fagot-Revurat, Y., and Malterre, D. (2007) *Nat. Nanotechnol.*, **2**, 617.

51 Rohart, S., Girard, Y., Nahas, Y., Repain, V., Rodary, G., Tejeda, A., and Rousset, S. (2008) *Surf. Sci.*, **602**, 28.

52 Rohart, S., Baudot, G., Repain, V., Girard, Y., Rousset, S., Bulou, H., Goyhenex, C., and Proville, L. (2004) *Surf. Sci.*, **559**, 47.

53 Repain, V., Rohart, S., Girard, Y., Tejeda, A., and Rousset, S. (2006) *J. Phys. Condens. Matter*, **18**, S17.

54 Boishin, G., Sun, L., Hohage, M., and Zeppenfeld, P. (2002) *Surf. Sci.*, **512**, 185.

55 Nahas, Y., Repain, V., Chacon, C., Girard, Y., and Rousset, S. (2010) *Surf. Sci.*, **604**, 829.

56 Venables, J. (2000) *Introduction to Surface and Thin Film Processes*, Cambridge University Press, Cambridge.

57 Brune, H. *et al.* (1999) *Phys. Rev. B*, **60**, 5991.

58 Venables, J., Bennett, P., Brune, H., Drucker, J., and Harding, J.H. (2003) *Philos. Trans. R. Soc. Lond. A*, **361**, 311.

59 Venables, J. (1997) *Phys. A*, **239**, 35.

60 Haas, G., Menck, A., Brune, H., Barth, J., Venables, J., and Kern, K. (2000) *Phys. Rev. B*, **61**, 11105.

61 Heim, K., Coyle, S., Hembree, G., and Venables, J. (1996) *J. Appl. Phys.*, **80**, 1161.

62 Amar, J.G. and Family, F. (1995) *Phys. Rev. Lett.*, **74**, 2066.

63 Hume-Rothery, W., Smallman, R.E., and Hayworth, C.W. (1969) *The Structure of Metals and Alloys*, The Metals and Metallurgy Trust, London.

64 Nielsen, L.P., Besenbacher, F., Stensgaard, I., Laegsgaard, E., Engdahl, C., Stolze, P., Jacobsen, K.W., and Norskov, J.K. (1993) *Phys. Rev. Lett.*, **71**, 754.

65 Neugebauer, J. and Scheffler, M. (1993) *Phys. Rev. Lett.*, **71**, 577.

66 Roeder, H., Schuster, R., Brune, H., and Kern, K. (1993) *Phys. Rev. Lett.*, **71**, 2086.

67 Oppo, S., Fiorentini, V., and Scheffler, M. (1993) *Phys. Rev. Lett.*, **71**, 2437.

68 Tersoff, J. (1995) *Phys. Rev. Lett.*, **74**, 434.

69 Thayer, G.E., Bartelt, N.C., Schmid, A.K., Bartelt, N.C., Asta, M., Hoyt, J.J., Chiang, S., and Hwang, R.Q. (2001) *Phys. Rev. Lett.*, **86**, 660.

70 Thayer, G.E., Bartelt, N.C., Ozolins, V., Schmid, A.K., Chiang, S., and Hwang, R.Q. (2002) *Phys. Rev. Lett.*, **89**, 036101.

71 Marathe, M., Imam, M., and Narasimhan, S. (2009) *Phys. Rev. B*, **79**, 085413.

72 Mehendale, S., Girard, Y., Repain, V., Chacon, C., Lagoute, J., Rousset, S., Marathe, M., and Narasimhan, S. (2010) *Phys. Rev. Lett.*, **105**, 056101.